

Integrated Optical MEMS for Scalable Trapped Ion Quantum Computing

*Daniel Klawson
Ming C. Wu*

Electrical Engineering and Computer Sciences
University of California, Berkeley

Technical Report No. UCB/EECS-2025-19

<http://www2.eecs.berkeley.edu/Pubs/TechRpts/2025/EECS-2025-19.html>

May 1, 2025



Copyright © 2025, by the author(s).
All rights reserved.

Permission to make digital or hard copies of all or part of this work for personal or classroom use is granted without fee provided that copies are not made or distributed for profit or commercial advantage and that copies bear this notice and the full citation on the first page. To copy otherwise, to republish, to post on servers or to redistribute to lists, requires prior specific permission.

Acknowledgement

The author would like to thank his many collaborators over the years for all their advice, mentorship, and guidance. In specific, thank you to the students, postdocs, and PIs of the Wu, Kanté, Sipahigil, Häffner, Mouradian, Campbell, and Hudson groups. This project is funded by the NSF Challenge Institute for Quantum Computation and the National Defense Science and Engineering Graduate Fellowship.

Integrated Optical MEMS for Scalable Trapped Ion Quantum Computing

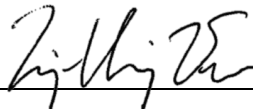
by Daniel Klawson

Research Project

Submitted to the Department of Electrical Engineering and Computer Sciences, University of California at Berkeley, in partial satisfaction of the requirements for the degree of **Master of Science, Plan II**.

Approval for the Report and Comprehensive Examination:

Committee:



Professor Ming C. Wu
Research Advisor

May 9, 2023

(Date)

* * * * *

Professor Boubacar Kanté
Second Reader

(Date)

Abstract

Quantum computing has emerged as a revolutionary field promising unprecedented computational power and transformative applications. Trapped ions have emerged as an encouraging platform for quantum computation due to their long coherence times, high-fidelity qubit operations, and the ability to achieve scalable entanglement and error correction. However, the practical realization of large-scale quantum systems faces significant challenges, including the need for efficient and scalable control of qubits. Integrated photonics has gained substantial attention as a promising platform for quantum computing – passive integrated photonics has shown potential for miniaturized, CMOS-compatible quantum computers on-a-chip. This thesis seeks to take a step further by integrating qubit select addressing and optical pulse generation on-chip using photonic micro electromechanical systems (MEMS). Through simulation and experimentation, the prospect of integrated MEMS for scaling trapped ion integrated circuits will be evaluated and critiqued. It is found that optical MEMS has the potential to further miniaturize ion trap quantum computers.

Table of Contents

1. Introduction	1
1.1. Quantum Computing	1
1.2. Integrated Photonics	2
2. Background	4
2.1. Project Goal	4
2.2. Optical Switching	5
3. System Components	7
3.1. Full System Overview	7
3.2. Optical Input	8
3.2.1. Fiber Array	8
3.2.2. Grating Coupling	9
3.3. Routing and Modulation	10
3.3.1. Waveguides	10
3.3.2. Optical Switch Design	11
3.3.2.1. Directional Coupler Switch	12
3.3.2.2. Adiabatic Coupler Switch	13
3.3.2.3. Reverse Coupler Switch	14
3.3.2.4. Performance Characterization	16
3.4. Qubit Excitation	17
3.5. Fabrication	19
3.6. Optical Packaging	21
4. Outlook	23

5. Conclusion	25
6. Acknowledgements	26
7. References	27

1. Introduction

1.1 Quantum Computing

Quantum computing is a new computing paradigm which can promise exponential computational speedup. With the ability to harness the fundamental principles of quantum mechanics, quantum computers have the potential to perform calculations that are practically infeasible for classical computers. Trapped ions have been identified as a leading approach in realizing a useful quantum computer, in addition to superconducting and photonic quantum bits (qubits) [1].

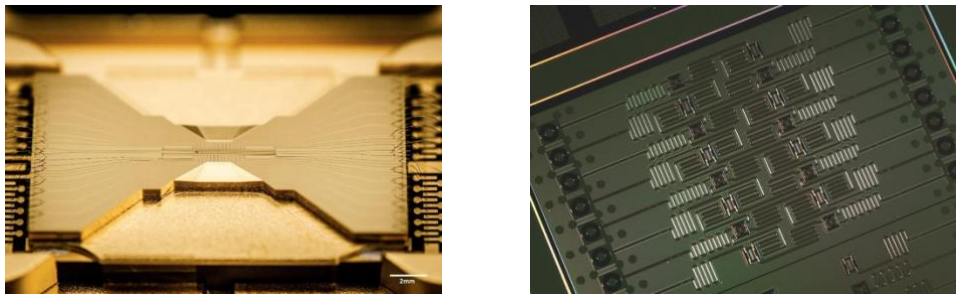


Figure 1: Trapped ion quantum processor (left, IonQ) versus a superconducting quantum processor (right, IBM) [2, 3]

Trapped ion systems offer several advantages, including long coherence times, high fidelity operations, and universality. These systems rely on the manipulation of the quantum states of individual trapped ions, confined within rotating electric and magnetic fields. This state manipulation is achieved through timed laser pulses resonant to the ion's atomic transition energies – single wavelength lasers cool, pump, entangle, and read-out the qubit within an ultra-high vacuum (UHV) chamber. At its core, an ion trap quantum computer requires full control over multiple wavelengths of light. This is traditionally accomplished through bulk optics.

However, near-term useful quantum algorithms require at least 50-100 qubits, while far-term, error corrected systems could require thousands [4]. This task becomes increasingly challenging with the size and instability of a tabletop optical system. Thus, integrated photonics has been identified as a viable method for scaling ion trap systems due to its size, scalability, and phase-stability.

1.2 Integrated Photonics

Integrated photonics is a technology platform which enables the control of light at the nanoscale, allowing the integration of optical components on a single, millimeter-size chip. It enables compact and scalable optical device engineering, made possible by CMOS-pioneered fabrication techniques. Integration of passive photonics with a 2-D surface electrode trap has showed massive promise for control of 1 to 2 qubits [5,6]. Optical waveguides and diffraction gratings were used to route and focus light from an input optical fiber to a trapped ion 50 μm from the surface of an integrated chip. This waveguide-grating-trap architecture has been demonstrated for full six-wavelength control of one $^{88}\text{Sr}^+$ ion, and single wavelength addressing of a pair of $^{40}\text{Ca}^+$ ions. These works set the foundation for waveguide integrated ion traps – yet, scaling to higher qubit systems with these architectures is still fundamentally limited.

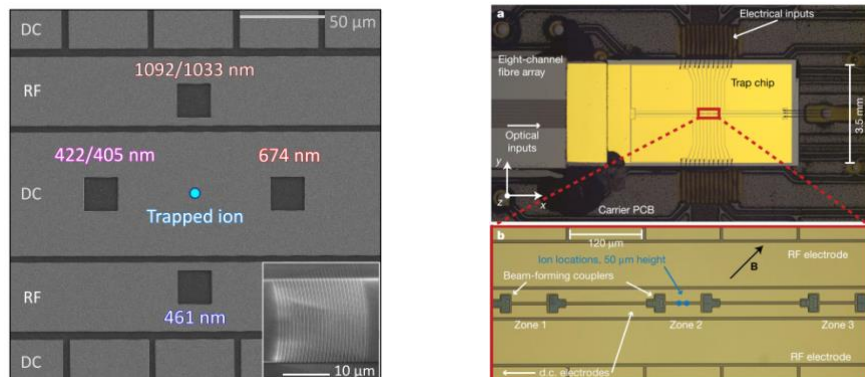


Figure 2: Single wavelength integrated optical control of two qubits (left) and multi-wavelength control of a single qubit (right) [5,6]

To scale towards and past noisy intermediate-scale quantum systems (NISQ), an integrated photonic ion trap quantum computer should be a ‘black box’ with only optical and electrical input/output (IO). Thus, all required components to realize an ion trap computer should be integrated. Preliminary groundwork has been laid in creating a ‘black box’ quantum computer – optical amplitude and frequency modulation, single photon detection, qubit excitation, optical routing, ion trapping, and CMOS control have all been envisioned on the same chip [7]. As mentioned previously, there have been a few seminal developments in integrated optical excitation via grating couplers. There has also been work in integrated photon detection – researchers have been able to count 370 nm photon emissions from trapped Yb ions through integrated single photon avalanche diodes (SPADs) and superconducting nanowire single photon detectors (SNSPDs) [8,9]. Yet, at the time of this writing, there has not yet been a demonstration of active photonic modulation or routing integrated on-chip with an ion trap.

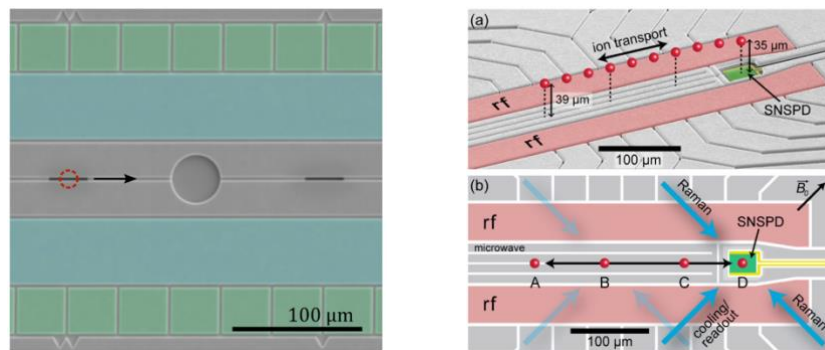


Figure 3: Trap integrated SPAD (left) SNSPD (right) [8,9].

This thesis will present designs and progress into a monolithically integrated ion trap chip with optical MEMS amplitude modulation and routing. Numerical simulations and experimental investigations were conducted to evaluate the performance of integrated photonic MEMS for single wavelength control of a $^{133}\text{Ba}^+$ qubit pair. Finally, an outlook will be presented on the usage of optical MEMS with ion trap quantum computing systems.

2. Background

2.1 *Project Goal*

A fully integrated system requires both optical routing and optical modulation – routing refers to ion select addressing, and modulation refers to pulse generation. The goal of this work is to investigate the feasibility of MEMS-based optical switching for ion trap systems. This thesis seeks to implement high fidelity one and two qubit gates for $^{133}\text{Ba}^+$ trapped ion pairs via a MEMS integrated $1.762\ \mu\text{m}$ quadrupole beam. Through this investigation, this work becomes a building block to higher qubit architectures.

One proposed quantum computing architecture is called the trapped-ion quantum charge-coupled device (QCCD). This architecture relies on single and multi-qubit operations on a chain of trapped ions. Typically separated by $\sim 5\ \mu\text{m}$ in pitch, a QCCD relies on optical and motional excitation to perform quantum computations. [10]. High fidelity gates require high fidelity optics; an integrated optical system must be able to generate and route light with high ON/OFF extinction ($> 30\ \text{dB}$) and fast rise/fall times ($\sim 1\ \mu\text{s}$). Therefore, the optical switch and excitation must be well engineered as to suppress crosstalk to neighboring ions.

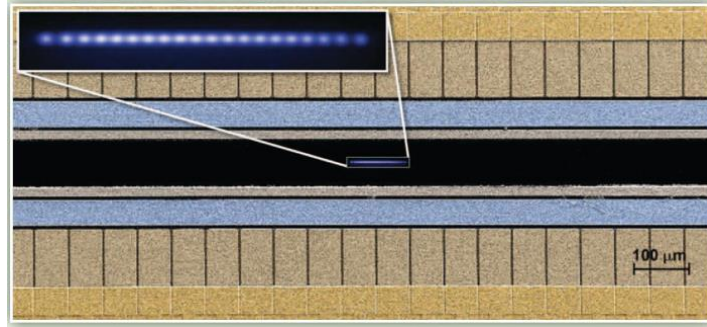


Figure 4: Trapped ion QCCD [10]

2.2 *Optical Switching*

Optical switches typically fall under a few categories: electro-optic, thermo-optic, and MEMS-based. Each of these methods have general tradeoffs, especially when the high-vacuum and low-temperature ion trap environment is considered. Electro-optic-based switches exploit the electro-optic effect, which involves changing the permittivity of a material under the influence of an applied electric field. These modulators typically employ materials like lithium niobate (LiNbO_3) or doped silicon (Si) with high electro-optic coefficients. By applying an electric field across the modulator, the phase or amplitude of a waveguide can be altered, allowing for fast optical switching.

Thermal-based switches utilize the thermal-optic effect, where changes in temperature induce variations in the refractive index of a material. These modulators typically consist of a heating element integrated with an optical waveguide. By controlling the temperature of the modulator, the refractive index can be altered, enabling modulation of the transmitted light via interference-based components such as Mach-Zehnder interferometers or ring resonators.

MEMS-based switches utilize microelectromechanical systems to induce mechanical movements that alter the position or properties of an optical waveguide. These modulators rely on the mechanical deformation of microscale structures, such as mirrors or waveguides, to

achieve modulation. By electrostatic actuation, the position of these structures can be controlled, routing the propagation of light. Through piezoelectric actuation, the refractive index of a waveguide can be controlled, allowing for interferometry based switching. A performance comparison of each architecture at room temperature can be seen in table 1 below [11].

Switch Type	Speed	Loss / Crosstalk	Power Consumption	Footprint
Electro-optic	High	Medium	Medium	High
Thermo-optic	Medium	Medium	High	Low
MEMS	Low	Low	Low	Medium

Table 1. General performance comparison of optical switching paradigms

When adapting an optical switch to be used at cryogenic-vacuum (4°K, 10^{-7} Torr), new considerations arise. For instance, thermo-optic switches become quite undesirable due to the introduction of excess heat into the chamber. Thus, thermo-optic switches can be ruled out for use with trapped ion qubits. Electro-optic modulators show some promise due to their capability for high-speed modulation. Recently, cryogenic switching in Silicon using the DC Kerr effect has been demonstrated via PIN phase shifters [12]. Gigahertz modulation speeds via a Mach-Zehnder interferometer (MZI) were achieved, although the design suffered from low extinction between the bar and cross states (10 dB).

MEMS-based switching via piezo-optomechanical coupling in aluminum nitride to silicon nitride has been demonstrated at 7°K. Underlying piezo-active AlN was used to strain Si₃N₄ ring resonators, enabling a change in refractive index due to the strain-optic effect and thus

a shift in resonance. Sub-microsecond switching time was achieved at ultra-low power, but the system also suffered from low extinction (10 dB) [13]. However, this design operated at 780 nm, one of the first works into shorter wavelength optical switching. Many of the wavelengths for trapped ions lie in the NUV – NIR spectrum, so this paper showed a promising step forward.

MEMS-waveguide-based optical switches show much poise in providing the optical routing and modulation for chip-scale ion trap devices. A 240 x 240 silicon switch was demonstrated to have close to 70 dB extinction, 0.04 dB / port loss, and sub-microsecond switching time at room temperature and atmosphere [14]. While the fabrication for this device was very complex, a simpler MEMS waveguide switch was shown to exhibit 28 dB extinction with a 15 μ s switching speed, values acceptable for use in ion trap systems, provided the performance translates in UHV [15].

This work proposes integrating a similar, single-layer SOI switch as demonstrated in [15] for 1.762 μ m operation. The next section will detail integration of this high extinction optical switch with a surface electrode trap and focusing grating couplers in a fully packaged system.

3. System Components

This section will first cover a high-level overview of the proposed, fully-packaged system. Then each optical component, starting from the input optical fiber all the way to the ion excitation, will be explained in detail. Electromagnetic simulation results as well as experimental outcomes will be presented and analyzed.

3.1 Full System Overview

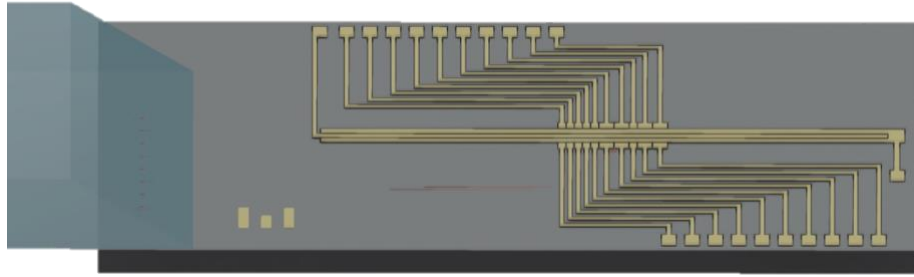


Figure 5: Digital rendering of the integrated photonic MEMS ion trap chip

A digital rendering of the optically packaged photonic circuit can be seen in figure 5. 1.762 μm light is injected via a fiber array to a row of grating couplers. The light is waveguided from the gratings to an optical switch array – to control a pair of ions, a 1 x 3 (input x output) switch matrix is used. When a switch cell is electrically actuated, the light is routed to a chosen waveguide towards a focusing grating coupler, which excites the trapped ion qubit. The 1 x 3 switch matrix allows for selection of one qubit addressing (tightly focused beam) or two qubit addressing (large global beam). The ions were assumed to be separated by 5 μm and at a height of 72 μm . In this demonstration, the 1.762 μm addressing beam is integrated. The cooling, pumping, shelving, and readout beams would be supplied via free space. Fluorescence detection would also be conducted over free space.

3.2 *Optical Input*

3.2.1 Fiber Array

Laser light is supplied to the chip from a fiber array via grating in-coupling. As the trapped ion PIC must work at UHV (10^{-9} Torr), special considerations must be taken with regards to fiber selection. To pump down to such high vacuum, the chamber is first baked out to 200°C to burn any outgassing organic contaminants. The ubiquitous SMF-28 optical fiber, most

broadly used in telecommunications but also acceptable for 1.762 μm wavelength, is rated to a maximum of 85°C. [16]. Thus, it would be unusable for UHV applications. The high temperature, polarization maintaining Fujikura SRSM15-PS-Y15 was selected as it can survive thermal cycling up to 300°C [17]. Polarization maintenance is also necessary for grating coupling, as the devices are functional only for TE polarization.

3.2.2 Grating Coupling

Grating couplers were designed via inverse design optimization to maximize single mode fiber coupling at 1.762 μm . The open-source package *EMopt* was used, a gradient descent based electromagnetic solver. The grating coupler pitch and etch separation were both parameterized as 10-parameter Fourier series expansions [18]. A Gaussian mode match to a $\sim 10 \mu\text{m}$ fiber mode served as the maximized figure of merit, and the Fourier coefficients a_i , b_i , c_i , and d_i were optimized. The parameterization can be seen below in equation 1.

$$\Lambda(i) = \sum_{i=1}^{N_F} \left[a_i \sin\left(\frac{\pi}{N_g} i\right) + b_i \sin\left(\frac{\pi}{N_g} i\right) \right]$$

$$w_g(i) = \sum_{i=1}^{N_F} \left[c_i \sin\left(\frac{\pi}{N_g} i\right) + d_i \sin\left(\frac{\pi}{N_g} i\right) \right]$$

Equation 1: Fourier series parameterization of grating pitch and etch width

The adjoint optimization resulted in a directionality of 62%, corresponding to a mode match of -3.5 dB. The large discrepancy in grating directionality and the mode match is due to the high angle – the optimal diffraction angle was found to be 33°. As the grating is built on 2 μm buried oxide SOI, the 34° angle corresponds to maximal constructive interference of the

bottom diffracted light trapped within the substrate. Thus, custom 28° total internal reflection (TIR) angle polished fiber arrays were used to supply 34° light onto the input couplers. An angle polish is necessary as the chip must have a low profile to fit within the UHV chamber.

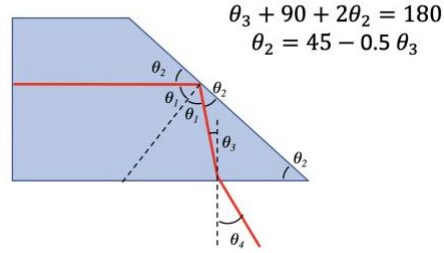


Figure 6: The operating principle of angle polished fiber. With index matched epoxy, $\theta_4 = \theta_3 = 34^\circ$, so $\theta_2 = 28^\circ$.

3.3 Routing and Modulation

3.3.1 Optical Waveguides

Low-loss single-mode ridge waveguides were used to guide light on-chip. The etch depth was chosen to be 70 nm and the ridge width was selected as 800 nm to ensure only the fundamental TE mode was supported. The electric field was also well confined to the silicon as to minimize propagation loss. The silicon was clad by 2 μm buried oxide and a 1 μm top oxide with 500 nm aluminum on top, which constituted the ion trap and switch electrodes. The buried oxide was fixed by the availability of 2 μm SOI, and the top oxide was chosen to be 1 μm as to be thick enough to prevent guided mode absorption into the top aluminum layer. Diagrams of the waveguide stack and the electric field intensity of the fundamental mode can be seen in figure 7.

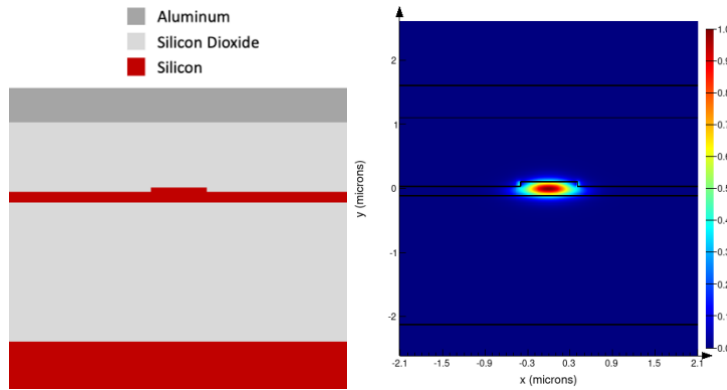


Figure 7: Material profile (left) and simulated E field intensity (right)

3.3.2 Optical Switch Design

A single layer SOI photonic MEMS switch was chosen to provide optical pulse generation and routing. Much like the architecture used in [15], electrostatic actuation was accomplished via a comb drive. The comb drive actuator consists of two sets of interdigitated comb-like structures, one fixed and the other movable, fabricated using CMOS nanofabrication techniques. The fixed comb structure is anchored to the substrate, while the movable comb structure is connected to a movable platform. By applying a voltage difference between the comb fingers, an electrostatic force is generated, leading to the movement of the movable comb structure towards or away from the fixed comb structure. This movement can be precisely controlled, allowing for actuation and positioning at the microscale.

In the optical switch, a coupler waveguide is connected to the comb-movable shuttle. When a voltage is applied, the coupler waveguide moves in proximity to a fixed bus waveguide. The waveguides were engineered to support a weakly confined mode – as the coupler waveguide approaches the bus waveguide, the mode is transferred via evanescent coupling. The waveguide couplers can be designed to support different coupling gaps, lengths, and strengths. In this work,

three different coupling designs were simulated in Lumerical Finite Difference Eigenmode, with each design carrying performance tradeoffs. A scanning electron micrograph (SEM) of the fabricated optical switch can be seen below

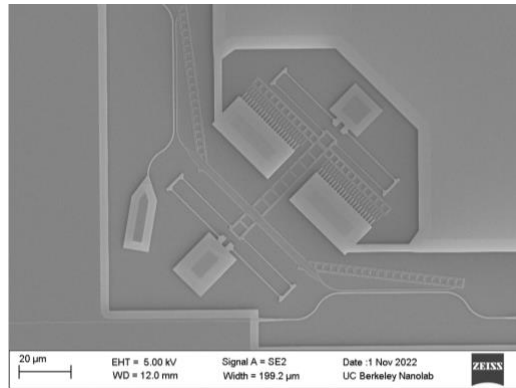


Figure 8: SEM of a fabricated optical switch

3.3.2.1 Directional Coupler Switch

The first design was a standard directional coupler. The coupler and bus waveguides were kept at a constant width of $0.620\ \mu\text{m}$. Because of this, the coupling gap must be controlled very precisely to exhibit high extinction switching. Electric field intensity of the directional coupler design at a $1\ \mu\text{m}$ and $0.15\ \mu\text{m}$ gaps can be seen below. At $0.15\ \mu\text{m}$, the energy jumps between the coupler and bus waveguide, illustrating one of the flaws with the directional coupler behavior.

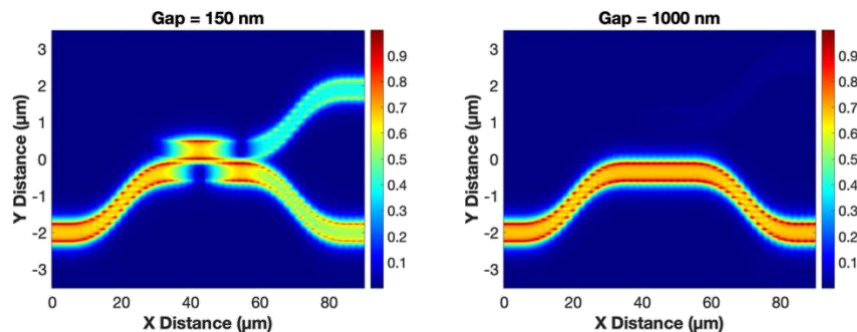


Figure 9: Electric field profiles of the directional coupler switch at 0.15 μm gap and 1 μm gap

The oscillatory nature of the directional coupler switch greatly inhibits its performance for use in trapped ions. High extinction (>30 dB) switching is a necessity – such extinction is only possible if the gap can be precisely controlled to an order of a few nanometers. Uncontrollable factors such as voltage source fluctuation and vibration could prevent precise actuation. Furthermore, UHV operation could cause ‘ringing’, or oscillation in the final coupling position due to a lack of damping. This issue will be discussed in detail at a later section, but in summary, the directional coupler architecture is unattractive for these many reasons.

3.3.2.2 Adiabatic Coupler Switch

The second design sought to counter the need for precise actuation by ensuring adiabatic energy transfer from coupler to bus waveguide. Both waveguides were gently tapered to ‘squeeze’ light from one to another. The bus waveguide, where light originates, was tapered down from a wide width to a narrow one. Therefore, the coupler waveguide was tapered up to match the effective index change in the mode. A 40 μm coupling length was chosen to allow for adiabatic transition and a coupling gap of 0.15 μm . Figure 10 shows electric field intensity plots for the OFF state and ON state of this switch design – extinction was simulated to be close to 40 dB.

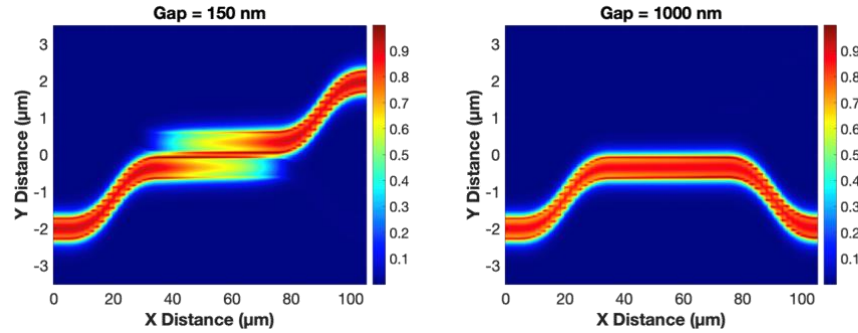


Figure 10: E-field in the ON state (left) and OFF state (right) for the adiabatic coupler

The adiabatic design guaranteed a smooth transfer of energy, and thus less need for precise gap control. Unity coupling was achieved in simulation for a 75 nm gap range, as compared to the 5 nm gap range with the directional coupler. As mentioned previously, this gap insensitivity is attractive for use with ions to enable high extinction vacuum operation. However, since the coupling works by moving two waveguides into proximity, stiction becomes a pertinent issue with operation. If too much voltage is applied, there is a risk of the coupler and waveguides crashing and becoming stuck, breaking the device. For trapped ion systems, sometimes vacuum pump down can take weeks – if the optical switch cannot survive long-haul performance, the utility is much limited.

3.3.2.3 Reverse Coupler Switch

The third design was implemented to compensate for the lack of precision in the directional coupler design and the threat of stiction in the adiabatic design. This design relied on adiabatic transition, but the actuation was reversed. In the previous two designs, when a potential is applied, the waveguides move closer. In this method, the MEMS actuator is reversed – as a bias is applied, the actuators move farther apart. This minimizes the risk of stiction, as the couplers could be designed to maximize the distance between the coupling waveguides.

For this system the 0 V state, which provided unity coupling, was designed to be at a 0.3 μm gap. For such a large gap, the coupler and bus waveguides had to be very narrow to yield strong enough evanescent coupling. So, mode confinement was very low and switching loss was expected to be relatively high. To achieve high extinction operation, a 2 μm waveguide gap was required, meaning the switching voltage would be higher than the directional or adiabatic designs. E field profiles of the ON and OFF states can be seen below.

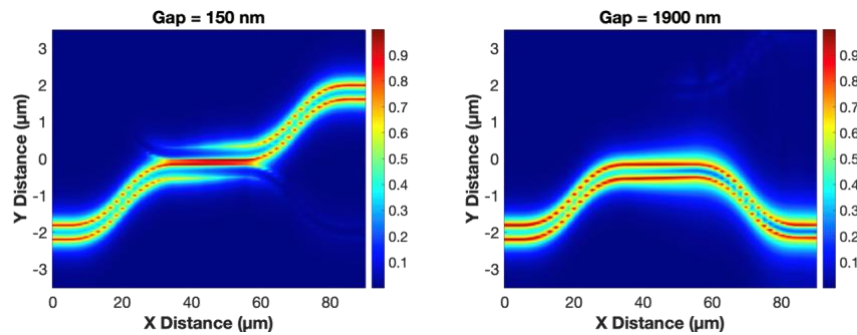


Figure 11: E-field in the OFF state (left) and ON state (right) for the reverse coupler

These three coupler designs each have their own advantages and disadvantages. While the directional coupler requires high precision actuation, it would be unlikely to achieve unity coupling through any fabrication error. The adiabatic coupler can achieve high extinction performance, but could be prone to stiction during operation. The reverse coupler seems to be the safest actuator, as it has minimal precision requirement and stiction risk, but it is lower extinction, higher voltage, and higher loss than the other two designs. Therefore, all three of these designs were fabricated and the best design for use with ions was chosen after testing in the lab.

Due to the limited commercial availability of the 1.762 μm laser, duplicate switch structures were created to operate at 1.55 μm . The coupling type and gap were kept constant with

the 1.762 designs, but the coupler dimensions were altered to replicate performance at 1.55 μm . Then, all the designs were tested in the lab to compare the performances.

3.3.2.4 Switch Characterization

The three optical switch designs were tested at 1.55 μm with DC electrostatic actuation. A fiber array was precisely aligned to a set of grating couplers with a Thorlabs 6-axis nano-positioner (MAX601D). A DC source supplied 0 to 20 volts to enable actuation. The actuation voltage for the gap-closing switch designs was calculated to be $\sim 13\text{V}$, which agreed with the experiment. Intensity images of switch actuation can be seen in the figure below.

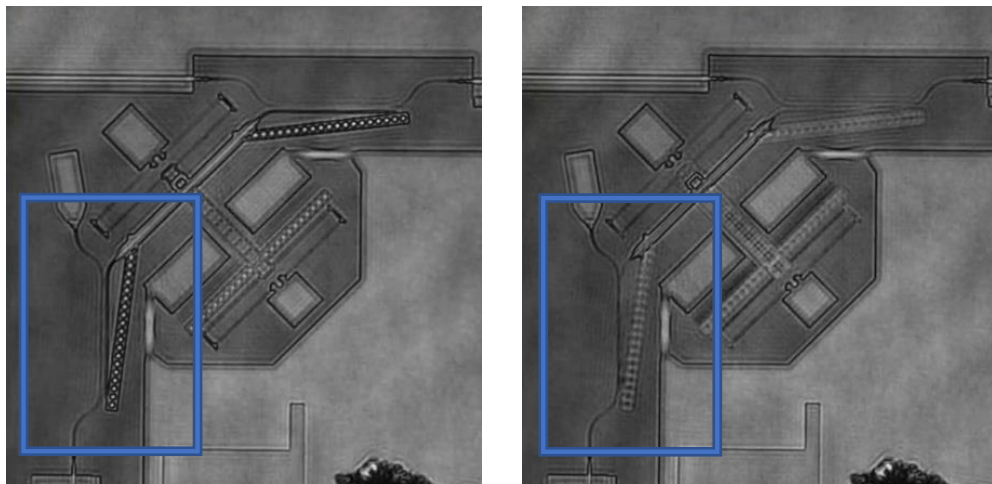


Figure 12: The optical switch at 0 V (left) and 14 V (right).

The adiabatic coupler design yielded the best results. With 14 V, the ON/OFF extinction was measured to be 28 dB. While the AC performance was not characterized, the actuator resonance was both calculated and simulated to be close to 70 kHz. This equates to an estimated

15 μs rise and fall time, which is acceptable for trapped ions. Therefore, the adiabatic coupler was selected to interface with the ions in the final package.

3.3 *Ion Excitation*

Focusing grating couplers were used to drive state transitions in the trapped ion qubits. As with the fiber couplers, inverse design optimization was used to create the grating profile in the propagation direction and maximize directionality. A Gaussian mode match was used as the figure of merit – unlike with the fiber couplers, the mode field diameter was fixed to 3 μm . The mode match height was set to a 72 μm , as that was the trapping height of the ion. A 70 nm partial etch was fixed and a 250 nm minimum feature size was enforced onto the parameterization. This represents the minimum feature size attainable through available 248 nm deep UV (DUV) lithography.

Since the ions require a tightly focused beam, two-dimensional focusing was employed by applying an elliptical curvature to the grating teeth in the transverse direction. Equation 2 below shows the grating line equation used [19].

$$m\lambda = n_{eff}\sqrt{x^2 + y^2} - xn_0\sin(\theta)$$

Equation 2: Elliptical focusing grating equation

Owing to the large transverse aperture and small propagation aperture, the beam shape is highly elliptical. Therefore, the gratings were laid out such that the trap axis corresponded with the tight transverse focusing. The spot size was 3 μm – crosstalk between the target ion and the neighboring ion 5 μm away was close to 30 dB. The optimized gratings were simulated to have

an emission angle of 34° and a directionality of 55%. A layout view with the E-field superimposed can be seen in figure 13. The triangular gratings on the left and right supply tightly focused, single-ion addressing beams. The rectangular grating on the bottom generates a $20\ \mu\text{m}$ global beam.

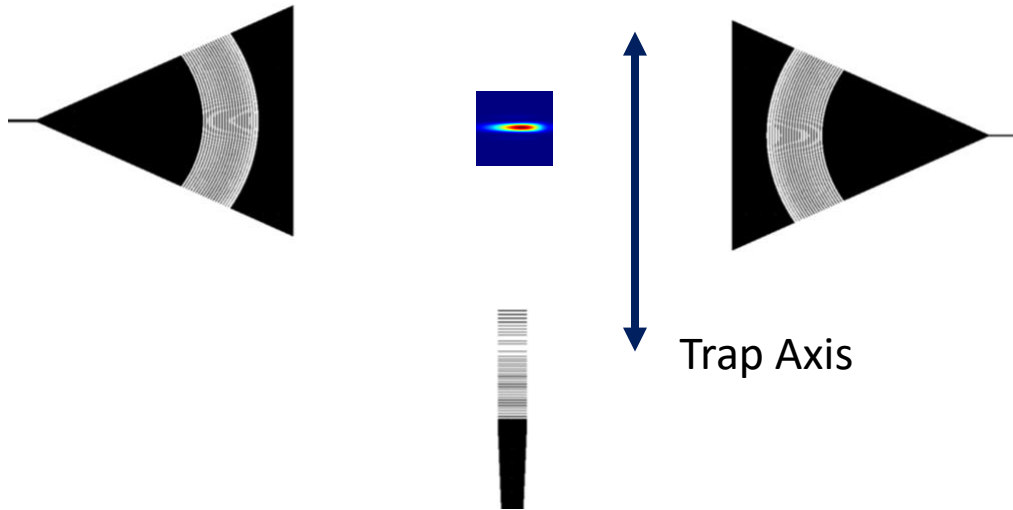


Figure 13: 2-qubit gate layout. The rightmost focusing grating is excited.

Although gratings are notoriously fabrication dependent, these elliptical beams, in conjunction with the mechanics of ion trapping, can withstand normal fabrication tolerance. The grating propagation direction is perpendicular to the trapping direction; in the case of over/under etch or over/under exposure, the grating angle would be most affected. Since the beam is elliptical, despite moderate angle deviation, power is still delivered effectively to the ions. This was verified through 3D FDTD simulation. If the beam were to shift along the axial direction of the trap, the ions can be shuttled by modulating the DC and RF potentials. So, this design mitigates performance loss due to reasonable expected fabrication error.

3.5 Fabrication

Three separate processes must be seamlessly integrated: passive photonics, MEMS, and the surface electrode ion trap. A 7-mask DUV lithography process was designed to fabricate all components compatibly. The flow can be seen in figure 14.

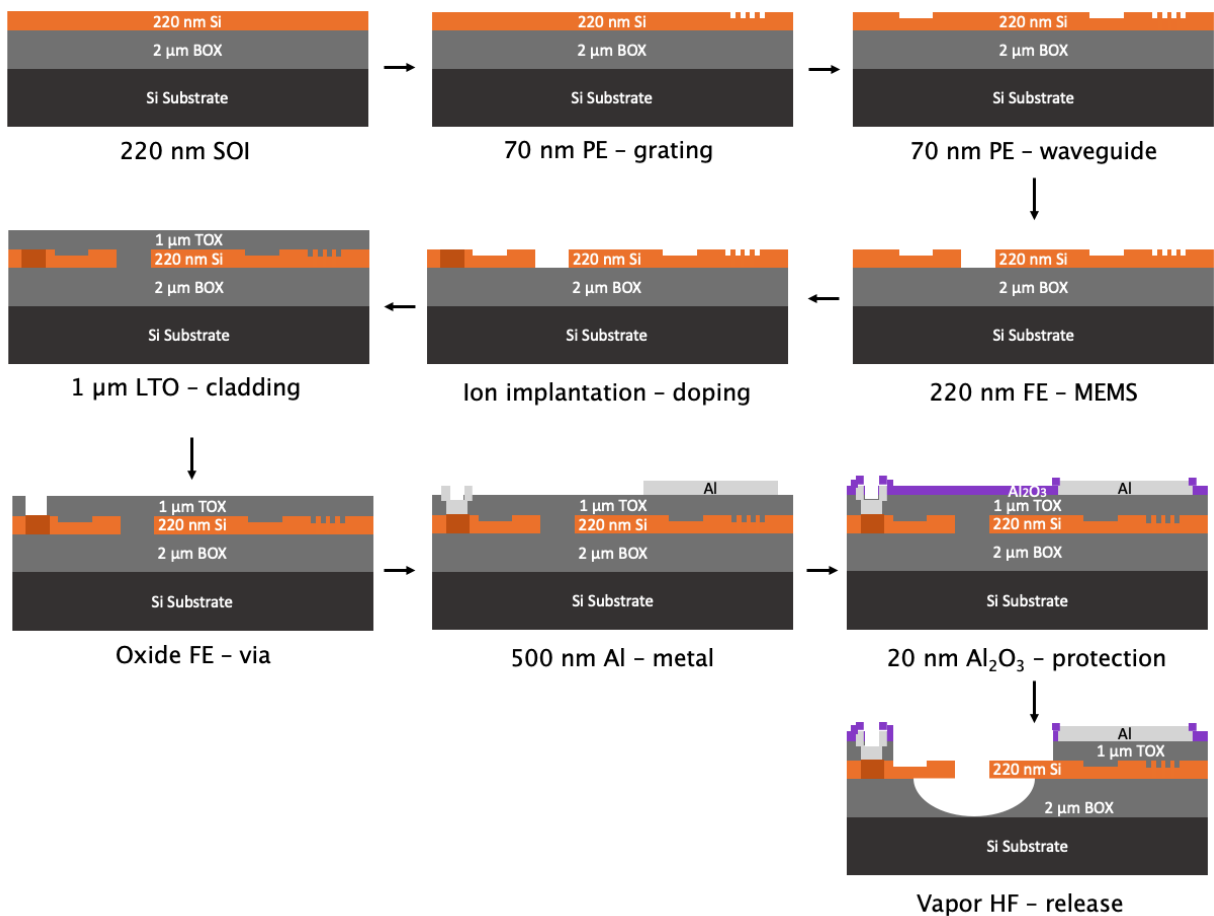


Figure 14: Device fabrication flow

The process starts with a 6-inch 220 nm SOI wafer. The first masking step is the grating coupler partial etch. This is a critical layer – with a minimum feature size of 250 nm, great care

was taken to calibrate the lithography dosage and timed etch. Next is the 70 nm waveguide partial etch. These features are on the order of 1 μm , so this step was kept separate from the previous due to aspect-ratio-dependent etching speed. The third and final silicon step came afterwards with a full 220 nm etch, stopped by the underlying oxide. This was also a crucial step, as the MEMS couplers had a critical dimension of 250 nm. Vertical sidewalls were also a necessity to ensure performance consistent with simulation. Then, the switch pads were p-doped via boron implantation to reduce the contact resistance and increase the switching speed. At this point, devices were released with vapor hydrofluoric acid (VHF) and tested in the lab.

After verifying the performance, the second half of processing could begin. A 1 μm low temperature oxide was grown via low pressure chemical vapor deposition (LPCVD). Vias to the underlining silicon switch pads were patterned and etched, allowing for electrical connections to the MEMS. Then, the aluminum ion trap and switch pad electrodes were lifted off with electron beam evaporation. The final deposition step was an atomic layer deposition (ALD) layer of aluminum oxide. At 20 nm thick, this layer served as a release protection layer – for the MEMS process, this step covered oxide areas that should not be undercut by the release etch. Finally, the wafer was diced, and individual MEMS die were released with VHF. A composite microscope image of a completed chip before VHF release is shown below. The entire chip is 5 by 14 mm.

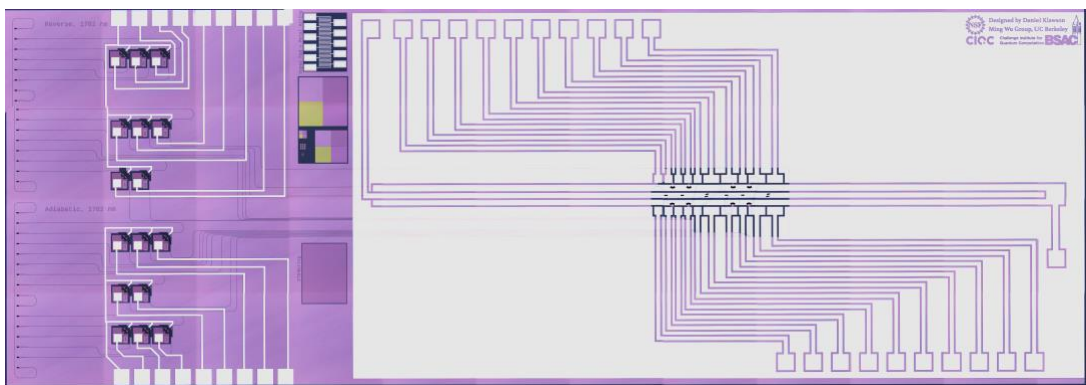


Figure 15: Fabricated chip-scale ion trap PIC

3.6 *Optical Packaging*

A serious challenge in the photonics industry is optical packaging. Light must be robustly injected with minimal loss and high mechanical stability. This becomes even more challenging when considering trapped ions – the packaged optics must survive UHV at the very least, and possibly cryogenic temperatures. At UHV, any trapped air or outgassing material can cause critical damage to a packaged device. At cryogenics, thermal expansion can cause unwanted forces and movement at the interfaces of materials. All these factors will cause a package to fail if it has not been engineered properly. Therefore, a two-stage epoxy methodology has been developed and tested to overcome cryo-vac conditions. Coupling was achieved at 4°K and 10^{-7} Torr, with the package surviving multiple thermal and atmospheric cycles and with minimal excess loss at cryo-vac.

An optical index-matched epoxy in conjunction with a low-outgassing epoxy was used to package a silicon photonics (SiPh) MEMS chip. The optical epoxy (Norland Optical Adhesive 146H) was used to bond the fiber array tip to a row of grating couplers. This epoxy is index matched to SiO₂ (n=1.46) and was dispensed pneumatically (FiconTec FL300) after coupling from fiber to grating was optimized. After aligning the fiber and dispensing the epoxy, it was UV cured and thermally crosslinked with a 60°C bake.

The optical epoxy by itself is not sufficient over long-term use. If the SiPh package is moved, there is great risk of the weak, thin optical epoxy breaking. Therefore, a second structural epoxy was used to attach the fiber array more securely. TRA-BOND 2151 was selected, as it is rated for high vacuum space applications by NASA [20]. This epoxy was applied by hand to the

fiber array glass v-groove block and cured through exposure to air for 24 hours. Images of the optical epoxy and structural epoxy package can be seen below.

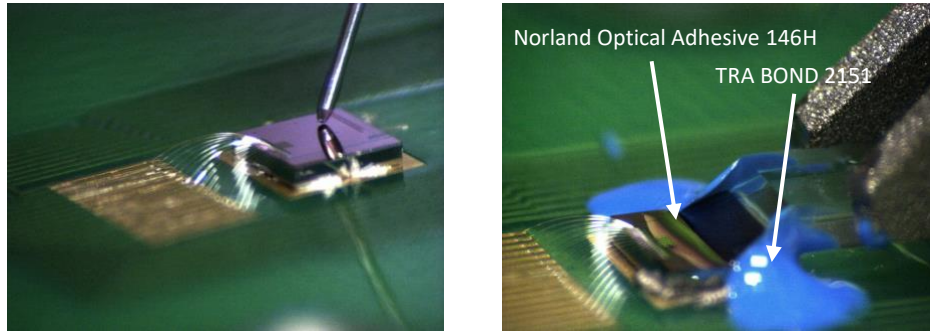


Figure 16: Dispensing the optical epoxy (left) and the dual-epoxy package (right)

The completed package was mounted in a cryostat for thermal cycling (Montana S200). Four SMF-28 fiber feedthroughs supplied tunable 1.31 μm light to the chip. Grating coupler loopbacks were measured before cooling, after cooling, and after warming. After warming, the package was inspected, cooled down and measured, then warmed again. The double-epoxy packaging scheme survived multiple thermal cycles with minimal variance in the coupling loss. The loss spectrum from atmosphere to the first cooling cycle can be seen in the figure below.

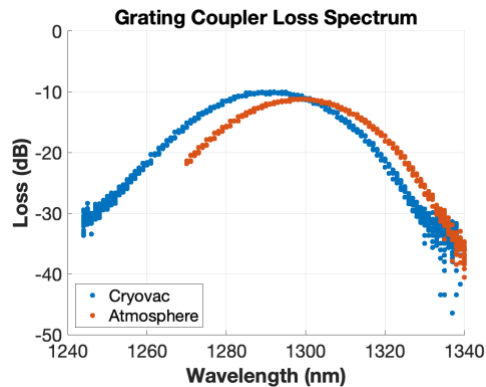


Figure 17: Loss spectrum of the grating coupler loopback at cryo-vac and at atmosphere

Surprisingly, the package exhibited 1 dB less loss at cryo-vac than at atmosphere. While the exact reason is unclear, it's possible that the package displaced mechanically to a more favorable position. Refractive index also changes versus temperature – it is also possible the index shifted slightly, which allowed for greater coupling. Further investigation is required to draw solid conclusions, but these results are promising.

4. Outlook

As of the time of writing, this chip has not been deployed to experiment on ions. There is doubt about the reliability of the MEMS design. Stiction is a huge risk – during fabrication, the yield was poor after the MEMS release. Even after optimizing the VHF process, it was rare to have 100% stiction-free release across the chip. This is due to the weakness of the single layer switch in the vertical direction. As the underlying oxide is etched away, the weakness of the switch and stress in the Si film causes much bending. If the bending is too much, the switch can get stuck to the handle silicon after all the oxide is etched away. To ensure a lower risk of stiction, it would be prudent to redesign the switch to have shorter released beams, increasing the stiffness in the downward direction. The fabrication process could also be augmented to reduce stress in the silicon film. This would limit the risk of stiction and increase the yield of the device.

Another concern for the switch performance is ringing. As mentioned previously, MEMS switches are mechanical resonators. When operating in UHV, any damping force supplied by the surrounding air is removed. This can cause oscillation in the position of the waveguide, and thus much fluctuation in the output optical signal. During the cryogenic packaging experiments

from the previous section, MEMS switching in cryo-vac was also tested. Vertical switch couplers based on two-layer Si were used – it was not the single layer SOI as proposed by this work, but in principle the results should be tractable [21]. When driven with a 50 kHz square pulse, the switch exhibited ON state ringing with a 3 MHz resonant frequency. The relaxation time greater than 10 μ s, greatly hindering the switching speed. A plot of optical signal and driving voltage vs time can be seen in figure 18.

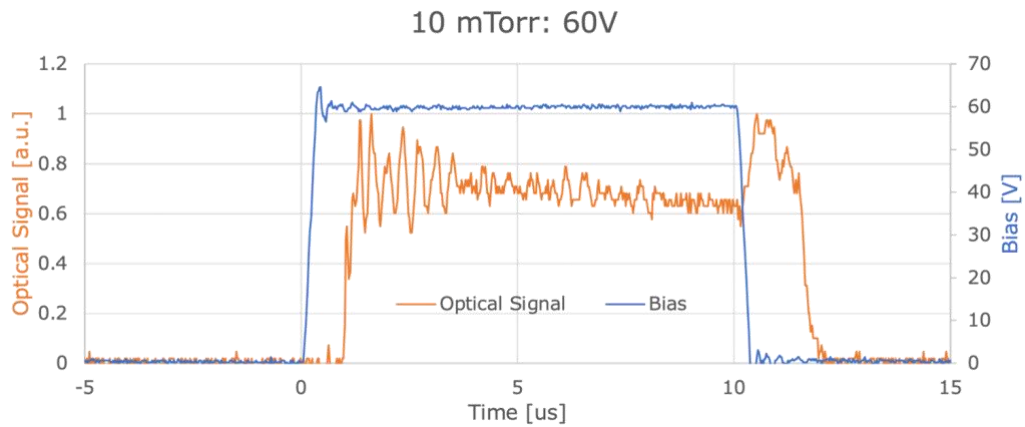


Figure 18: Ringing observed in vertical parallel plate MEMS actuation

As this switch uses parallel plate actuation, ringing effects would be expected to be less pronounced as a comb drive switch. So, it can be expected that this proposed switch design would suffer from more serious effects than this tested device. It is known that custom driving waveforms can be used to mitigate ringing, but these were not investigated in this work, and nor are they perfect.

Despite the ringing and stiction effects, the optical MEMS switch could be used for on-chip routing rather than modulation. Qubit selection would not necessarily need to be at μ s speed – therefore, the high-speed ringing effects would be minimized with just DC, steady-state

actuation. Furthermore, the device could be re-designed to minimize ringing by adding on-chip damping and feedback control. With these changes in mind, MEMS modulation is still an attractive prospect for scaling ion trap quantum computing.

5. Conclusion

In conclusion, this thesis has explored the possibility of optical MEMS for modulation and routing of light for chip-scale ion trap quantum computers. Through electromagnetic simulation and experimentation, MEMS switching and qubit optical excitation was explored and critiqued. Additionally, a fully functional chip was fabricated and showcased, with the capability of controlling a pair of qubits with an integrated $1.762\ \mu\text{m}$ beam. Then, a novel cryogenic vacuum packaging methodology was presented and evaluated with promising results. Finally, an outlook on this work and the nascent field of photonic MEMS integrated ion trapping was presented.

6. Acknowledgements

The author would like to thank his many collaborators over the years for all their advice, mentorship, and guidance. In specific, thank you to the students, postdocs, and PIs of the Wu, Kanté, Sipahigil, Häffner, Mouradian, Campbell, and Hudson groups. This project is funded by the NSF Challenge Institute for Quantum Computation and the National Defense Science and Engineering Graduate Fellowship.

7. References

- [1] C. Monroe and J. Kim, “Scaling the ion trap quantum processor,” *Science* (80-.), vol. 339, no. 6124, pp. 1164–1169, 2013, doi: 10.1126/science.1231298.
- [2] IONQ. “Trapping an Ion”. (Aug. 25, 2021). Accessed: May 6, 2023. [Online Image]
- [3] IBM. “Testing Next-Gen Qubits”. (Sep. 25, 2018). Accessed: May 6, 2023. [Online Image]
- [4] J. Preskill, “Quantum computing in the NISQ era and beyond,” *Quantum*, vol. 2, no. July, pp. 1–20, 2018, doi: 10.22331/q-2018-08-06-79.
- [5] R. J. Niffenegger *et al.*, “Integrated optical control and enhanced coherence of ion qubits via multi-wavelength photonics,” pp. 1–9, 2020, [Online]. Available: <http://arxiv.org/abs/2001.05052>.
- [6] K. K. Mehta, C. Zhang, M. Malinowski, T.-L. Nguyen, M. Stadler, and J. P. Home, “Integrated optical multi-ion quantum logic,” 2020, [Online]. Available: <http://arxiv.org/abs/2002.02258>.
- [7] G. Moody *et al.*, “2022 Roadmap on integrated quantum photonics,” *JPhys Photonics*, vol. 4, no. 1, 2022, doi: 10.1088/2515-7647/ac1ef4.
- [8] W. J. Setzer *et al.*, “Fluorescence detection of a trapped ion with a monolithically integrated single-photon-counting avalanche diode,” *Appl. Phys. Lett.*, vol. 119, no. 15, 2021, doi: 10.1063/5.0055999.
- [9] S. L. Todaro *et al.*, “State Readout of a Trapped Ion Qubit Using a Trap-Integrated Superconducting Photon Detector,” *Phys. Rev. Lett.*, vol. 126, no. 1, p. 10501, 2021, doi: 10.1103/PhysRevLett.126.010501.
- [10] J. M. Pino *et al.*, “Demonstration of the QCCD trapped-ion quantum computer architecture,” 2020, [Online]. Available: <http://arxiv.org/abs/2003.01293>.
- [11] W. In, “Optical Switching Technology Comparison: Optical MEMS vs Other Technologies,” *IEEE Optical Communications*, November, pp. 23–29, 2003.
- [12] U. Chakraborty *et al.*, “Cryogenic operation of silicon photonic modulators based on the DC Kerr effect,” *Optica*, vol. 7, no. 10, p. 1385, 2020, doi: 10.1364/optica.403178.
- [13] P. R. Stanfield, A. J. Leenheer, C. P. Michael, R. Sims, and M. Eichenfield, “CMOS-compatible, piezo-optomechanically tunable photonics for visible wavelengths and

- cryogenic temperatures,” *Opt. Express*, vol. 27, no. 20, p. 28588, 2019, doi: 10.1364/oe.27.028588.
- [14] T. J. Seok, K. Kwon, J. Henriksson, J. Luo, and M. C. Wu, “Wafer-scale silicon photonic switches beyond die size limit,” *Optica*, vol. 6, no. 4, p. 490, 2019, doi: 10.1364/optica.6.000490.
- [15] S. Han *et al.*, “ 32×32 silicon photonic MEMS switch with gap-adjustable directional couplers fabricated in commercial CMOS foundry,” *J. Opt. Microsystems*, vol. 1, no. 02, pp. 1–9, 2021, doi: 10.1117/1.jom.1.2.024003.
- [16] Corning, “SMF-28 ULL Optical Fiber,” PI1470 datasheet, July 2014
- [17] Fujikura, “Polyimide coated PANDA,” SRSM15-PS-Y15 datasheet
- [18] A. Michaels and E. Yablonovitch, “Inverse design of near unity efficiency perfectly vertical grating couplers,” *Opt. Express*, vol. 26, no. 4, p. 4766, 2018, doi: 10.1364/oe.26.004766.
- [19] L. Cheng, S. Mao, Z. Li, Y. Han, and H. Y. Fu, “\Grating Couplers on Silicon Photonics: Design Principles, Emerging Trends and Practical Issues (Micromachines (2020), 11, 666),” *Micromachines*, vol. 13, no. 4, 2022, doi: 10.3390/mi13040606.
- [20] NASA, “Outgassing Data Introduction,” TRA-BOND 2151 datasheet
- [21] T. J. Seok, N. Quack, S. Han, R. S. Muller, and M. C. Wu, “Large-scale broadband digital silicon photonic switches with vertical adiabatic couplers,” *Optica*, vol. 3, no. 1, p. 64, 2016, doi: 10.1364/optica.3.000064.